

sensitive to light elements such as boron (29), revealed a planar structure (indicated by a purple arrow) at this interface. The observed contrast and structure are consistent with a simulated ABF image of the borophene structure model (Fig. 3C). Measured sheet thicknesses of ~0.27 to ~0.31 nm match both the monolayer structure model and multiwalled boron nanotubes (15).

X-ray photoelectron spectroscopy (XPS) measures both sample composition and the oxidation state of the species present. Although the borophene islands persisted under ambient conditions (fig. S12), the emergence of higher-binding energy features in the XPS B 1s core-level spectra (Fig. 3D) demonstrate that bare samples (black curve) were partially oxidized within several hours in ambient conditions. However, this oxidation was impeded by an amorphous silicon/silicon oxide capping layer (red curve), which delayed oxidation for several weeks (blue curve). The unoxidized, capped sample is fit by two Voigt components, which reflect the differences in chemical environment between the low- and high-buckled atoms. Increasing the photoelectron detector angle from the sample normal enhances XPS surface sensitivity, thereby selectively probing the surface and subsurface. The normalized, integrated components of angle-resolved XPS spectra on silicon-capped borophene are plotted in Fig. 3E. With increasing emission angle, the relative intensities of the carbon, silicon, and boron peaks increased, whereas the silver peak diminished. These results confirm the structure shown in the inset schematic, corroborating our AES, STM, and STEM results. Additional XPS data are given in fig. S13.

As shown above, theoretical predictions of the borophene structure forecast metallic characteristics. However, all known bulk boron allotropes are semiconductors at standard conditions, only becoming metallic at extremely high pressures (17). Scanning tunneling spectroscopy (STS) confirms the metallic characteristics of borophene through  $I$ - $V$  curves (Fig. 4A) and  $dI/dV$  spectra (which measure the local electronic DOS, Fig. 4B). These show gapless (i.e., metallic) behavior consistent with the superposition between the Ag(111) surface (30) and the predicted filled-state population in borophene (Fig. 2G). These observations are likely to motivate and inform further studies of metallicity and related phenomena in 2D boron polymorphs.

## REFERENCES AND NOTES

1. T. Ogitsu, E. Schwegler, G. Galli, *Chem. Rev.* **113**, 3425–3449 (2013).
2. B. Douglas, S.-M. Ho, *Structure and Chemistry of Crystalline Solids* (Springer Science & Business Media, New York, 2007).
3. A. R. Oganov *et al.*, *Nature* **457**, 863–867 (2009).
4. H.-J. Zhai, B. Kiran, J. Li, L.-S. Wang, *Nat. Mater.* **2**, 827–833 (2003).
5. A. P. Sergeeva *et al.*, *Acc. Chem. Res.* **47**, 1349–1358 (2014).
6. H.-J. Zhai *et al.*, *Nat. Chem.* **6**, 727–731 (2014).
7. Z. A. Piazza *et al.*, *Nat. Commun.* **5**, 3113 (2014).
8. I. Boustani, *Phys. Rev. B* **55**, 16426–16438 (1997).
9. H. Tang, S. Ismail-Beigi, *Phys. Rev. Lett.* **99**, 115501 (2007).
10. X.-F. Zhou *et al.*, *Phys. Rev. Lett.* **112**, 085502 (2014).
11. K. C. Lau, R. Pandey, *J. Phys. Chem. C* **111**, 2906–2912 (2007).
12. E. S. Penev, S. Bhowmick, A. Sadrzadeh, B. I. Yakobson, *Polymorphism of Two-Dimensional Boron*, **12**, 2441–2445 (2012).
13. Y. Liu, E. S. Penev, B. I. Yakobson, *Angew. Chem. Int. Ed.* **52**, 3156–3159 (2013).
14. H. Liu, J. Gao, J. Zhao, *Sci. Rep.* **3**, 3238 (2013).
15. F. Liu *et al.*, *J. Mater. Chem.* **20**, 2197 (2010).
16. H. Okamoto, *J. Phase Equilibria* **13**, 211–212 (1992).
17. M. I. Erements, V. V. Struzhkin, H. Mao, R. J. Hemley, *Science* **293**, 272–274 (2001).
18. Additional supplementary text and data are available on Science Online.
19. B. Kiraly *et al.*, *Nat. Commun.* **4**, 2804 (2013).
20. S. Berner *et al.*, *Angew. Chem.* **46**, 5115–5119 (2007).
21. F. Müller *et al.*, *Phys. Rev. B* **82**, 113406 (2010).
22. H. I. Rasool *et al.*, *J. Am. Chem. Soc.* **133**, 12536–12543 (2011).
23. A. R. Oganov, C. W. Glass, *J. Chem. Phys.* **124**, 244704–244716 (2006).
24. Q. Zhu, L. Li, A. R. Oganov, P. B. Allen, *Phys. Rev. B* **87**, 195317 (2013).
25. A. Kolmogorov, S. Curtarolo, *Phys. Rev. B* **74**, 224507 (2006).
26. B. Feng *et al.*, *Nano Lett.* **12**, 3507–3511 (2012).
27. C. Lee, X. Wei, J. W. Kysar, J. Hone, *Science* **321**, 385–388 (2008).
28. Q. Guo *et al.*, *Surf. Sci.* **604**, 1820–1824 (2010).
29. R. Ishikawa *et al.*, *Nat. Mater.* **10**, 278–281 (2011).
30. J. Klewer *et al.*, *Science* **288**, 1399–1402 (2000).

## ACKNOWLEDGMENTS

This work was performed, in part, at the Center for Nanoscale Materials, a U.S. Department of Energy Office of Science User Facility under Contract No. DE-AC02-06CH11357. This work was also performed, in part, at the NUANCE Center, supported by the

International Institute for Nanotechnology, Materials Research Science and Engineering Centers (NSF DMR-1121262), the Keck Foundation, the State of Illinois, and Northwestern University. A.J.M., B.K., J.D.W., X.L., J.R.G., M.C.H., and N.P.G. acknowledge support by the U.S. Department of Energy SISGR (contract no. DE-FG02-09ER16109), the Office of Naval Research (grant no. N00014-14-1-0669), and the National Science Foundation Graduate Fellowship Program (DGE-1324585 and DGE-0824162). X.-F.Z. thanks the National Science Foundation of China (grant no. 11174152), the National 973 Program of China (grant no. 2012CB921900), and the Program for New Century Excellent Talents in University (grant no. NCET-12-0278). U.S. thanks the National Council of Science and Technology, CONACyT (proposal no. 250836). A.R.O. acknowledges support from the Defense Advanced Research Projects Agency (grant no. W31P4Q1210008) and the Government of Russian Federation (no. 14.A12.31.0003). D.A., M.J.Y., and A.P. acknowledge support by the National Institute on Minority Health and Health Disparities (NIMHD) in the program Research Centers in Minority Institutions Program (RCMI) Nanotechnology and Human Health Core (grant G12MD007591), the NSF PREM DMR (grant no. DMR-0934218), the Welch Foundation (grant no. AX-1615), and the Department of Defense (grant no. 64756-RT-REP).

## SUPPLEMENTARY MATERIALS

www.sciencemag.org/content/350/6267/1513/suppl/DC1  
Materials and Methods  
Supplementary Text  
Figs. S1 to S13  
References (31–57)

27 July 2015; accepted 28 October 2015  
10.1126/science.aad1080

## BATTERIES

# Visualization of O-O peroxo-like dimers in high-capacity layered oxides for Li-ion batteries

Eric McCalla,<sup>1,2,3,4</sup> Artem M. Abakumov,<sup>5,6</sup> Matthieu Saubanière,<sup>2,3,7</sup> Dominique Foix,<sup>2,3,8</sup> Erik J. Berg,<sup>9</sup> Gwenaelle Rousse,<sup>1,3,10</sup> Marie-Liesse Doublet,<sup>2,3,7</sup> Danielle Gonbeau,<sup>2,3,8</sup> Petr Novák,<sup>9</sup> Gustaaf Van Tendeloo,<sup>5</sup> Robert Dominko,<sup>4</sup> Jean-Marie Tarascon<sup>1,2,3,10\*</sup>

Lithium-ion (Li-ion) batteries that rely on cationic redox reactions are the primary energy source for portable electronics. One pathway toward greater energy density is through the use of Li-rich layered oxides. The capacity of this class of materials (>270 milliampere hours per gram) has been shown to be nested in anionic redox reactions, which are thought to form peroxo-like species. However, the oxygen-oxygen (O-O) bonding pattern has not been observed in previous studies, nor has there been a satisfactory explanation for the irreversible changes that occur during first delithiation. By using Li<sub>2</sub>IrO<sub>3</sub> as a model compound, we visualize the O-O dimers via transmission electron microscopy and neutron diffraction. Our findings establish the fundamental relation between the anionic redox process and the evolution of the O-O bonding in layered oxides.

**B**ecause lithium-ion (Li-ion) batteries have the highest energy density of all commercially available batteries, they are able to power most consumer electronics and have emerged as the technology of choice for powering electric vehicles. Li-ion batteries may also be used for grid storage and load-leveling for renewable energy. Current state-of-the-art positive electrodes use layered rock salt oxides (LiCoO<sub>2</sub> and its derivatives), spinel (LiMn<sub>2</sub>O<sub>4</sub>), or polyanionic compounds such as olivine-type LiFePO<sub>4</sub> (1). One

push to increase the practical capacity limit of LiCoO<sub>2</sub> is via chemical substitution aimed at stabilizing the layered framework. The partial replacement of Co<sup>3+</sup> with Ni<sup>2+</sup> and Mn<sup>4+</sup> has led to the Li(Ni<sub>x</sub>Mn<sub>y</sub>Co<sub>1-x-y</sub>)O<sub>2</sub> layered oxides being coined as stoichiometric nickel manganese cobalt (NMC) oxides. These compounds have improved safety and capacities approaching 200 mA-hour/g. Further substitution of the transition metals by Li results in capacities exceeding 270 mA-hour/g. These materials are referred to as Li-rich layered

oxides, as some Li ions now occupy crystallographic sites in the transition metal layers in the ordered rock salt structure (2, 3). During the first charge, these compounds undergo a transformation such that subsequent charge-discharge curves take an S shape without clear redox plateaus (as seen for  $\text{Li}_2\text{Ir}_{0.75}\text{Sn}_{0.25}\text{O}_3$  in Fig. 1C). Partial oxidation of the oxygen sublattice upon Li removal, leading to an increased capacity, has been conjectured (4–12). The high capacity is rooted in the cumulative reversibility of both cationic and anionic redox processes ( $2\text{O}^{2-} \rightarrow \text{O}_2^{n-}$ , where  $n = 1, 2, \text{ or } 3$ ) (13–15). We speculated, but did not observe, that this oxidation of oxygen results in the formation of peroxo-like species with shortened O–O distances. Nevertheless, such studies demonstrate that the Li–(de)intercalation chemistry does not rely solely on cationic redox reactions as the source of energy storage; **the oxygen sublattice is active as well.**

Such O–O pairing in the oxygen lattice, resulting from the formation of  $\text{O}_2^{n-}$  species, predominantly occurs in compounds that have highly covalent metal–oxygen bonding—that is, systems showing a high degree of  $\text{M}(\text{d})\text{--O}(\text{sp})$  band overlap (13–16). Although this description of the oxidation of the oxygen sublattice is relatively new, the activity of the anionic network for chalcogenide (Ch)–based electrodes has long been recognized (17). By properly selecting cation–anion pairs, Rouxel showed the feasibility of tuning the degree of the metal  $\text{M}(\text{3d})\text{--Ch}(\text{sp})$  band mixing so as to trigger the formation of S–S dimers or Te–Te–Te trimers, as observed for iridium tellurides (17). Moreover, by performing a survey of various compounds such as  $\text{Li}_2\text{Ru}_{1-x}\text{Sn}_x\text{O}_3$  (13),  $\text{Li}_{4/27}\text{Fe}_{0.56}\text{TeO}_6$  (16),  $\text{Li}_4\text{NiTeO}_6$  (18), and  $\text{Li}_4\text{FeSbO}_6$  (19), we have demonstrated that the stability of the oxygen close-packed framework against  $\text{O}_2$  evolution at high potential is highly tunable with composition. This finding is particularly important because this process leads to large irreversible capacities and poor long-term cycling (16, 19, 20). Layered compounds containing 4d metals have recently been shown to have reversible capacities of 300 mA-hour/g that involve a reversible anionic redox process (21). There is no direct structural evidence for the presence of peroxo-like species in any layered oxide, nor is it clear to

what extent oxygen can be reversibly oxidized (i.e., the value of  $n$  in  $\text{O}_2^{n-}$  remains an enigma).

We address these questions via a model system consisting of a Li-rich layered phase with Ir as a 5d metal so as to increase the covalency and minimize the unwanted cationic migration during charge-discharge cycling with the larger Ir atoms.  $\text{Li}_2\text{Ir}_{1-x}\text{Sn}_x\text{O}_3$  compounds with  $x = 0, 0.25$ , and  $0.5$  were prepared as described in the supplementary materials (22). Figure 1A (left) shows the structure of pristine  $\text{Li}_2\text{IrO}_3$ , which displays the cubic close-packed O3 stacking of the Li layers and the  $\text{Li}_{1/3}\text{Ir}_{2/3}\text{O}_2$  slabs, where each Li cation is surrounded by six Ir cations to form a honeycomb-

like ordering pattern. Figure 1B and fig. S1 show x-ray powder diffraction (XRD) patterns of the pristine  $\text{Li}_2\text{Ir}_{1-x}\text{Sn}_x\text{O}_3$  materials and demonstrate typical shifts in peak positions consistent with a solid solution, confirmed by the progression of lattice parameters seen in table S1. Figure 1, C and D, and fig. S2 show the electrochemical performance of the  $x = 0, 0.25$ , and  $0.5$  materials. The  $x = 0.25$  and  $0.5$  samples show cycling behavior typical of Li-rich oxides: two plateaus on first charge in the graphs of voltage versus  $y$  in  $\text{Li}_y\text{Ir}_{1-x}\text{Sn}_x\text{O}_3$ , with a transformation taking place such that the second charge cycle is markedly different from the first, with an S shape now visible.

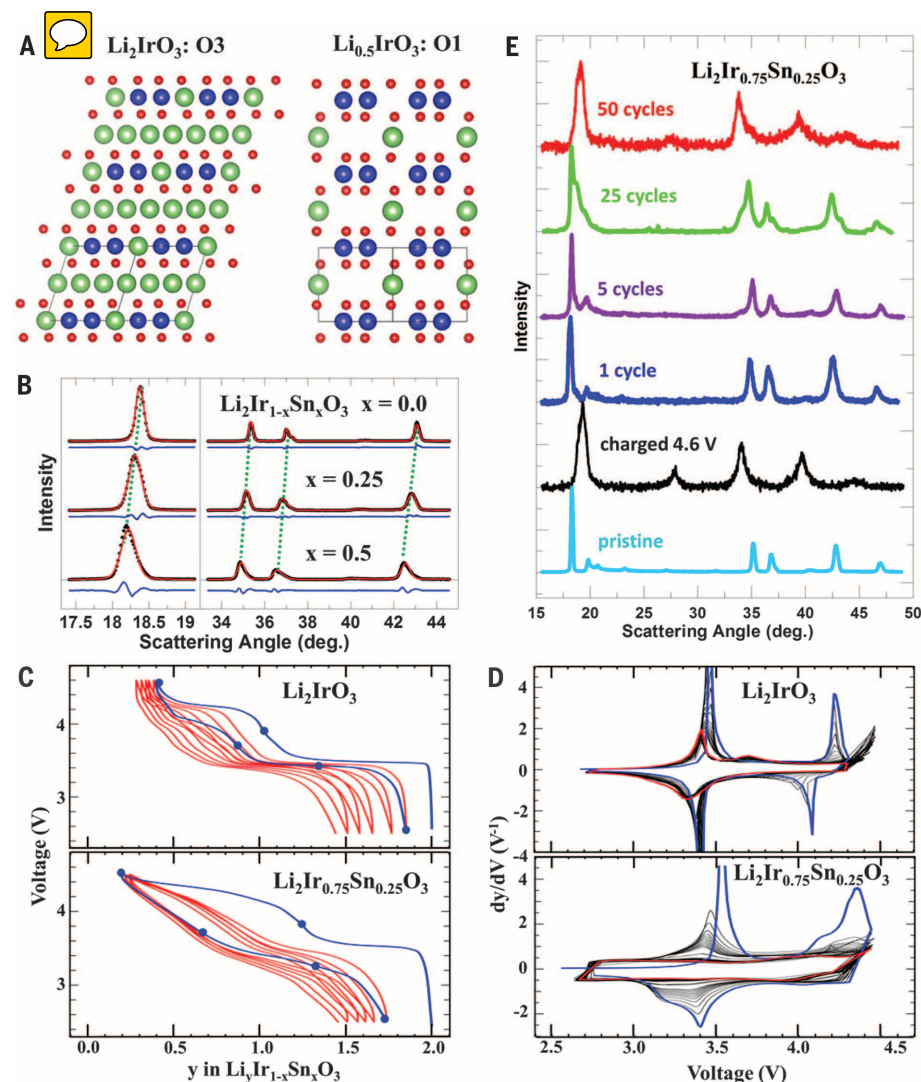


**Fig. 1. Structural transformations and electrochemical cycling of Li-Ir-Sn-O materials.** (A) (Left) Structure of the pristine  $\text{Li}_2\text{IrO}_3$  material, showing the O3 stacking. (Right) Structure of the fully charged material, showing the O1 stacking. Both structures are shown in the [110] projection. Throughout the figures Ir is blue, Li is green, and O is red. (B) XRD patterns for the pristine materials with varying Sn content, fitted by taking stacking faults into account with the FAULTS software. Green dashed lines show peak shifts, consistent with an increase in cell volume as Sn content increases. Complete patterns are included in fig. S1. (C) Voltage curves showing the first 10 cycles at C/10 between 2.5 and 4.6 V. The first cycle shown in blue, and blue circles represent specific compositions, as referred to in Fig. 2D. (D) Derivative curve showing the evolution of the redox peaks between the first (blue) and 50th (red) cycles. (E) XRD patterns for  $\text{Li}_2\text{Ir}_{0.75}\text{Sn}_{0.25}\text{O}_3$  after various electrochemical tests, showing a gradual conversion during extended cycling until the final scan looks similar to that of the first charged sample.

<sup>1</sup>Collège de France, Chimie du Solide et de l'Énergie, FRE 3677, 11 Place Marcelin Berthelot, 75231 Paris Cedex 05, France. <sup>2</sup>ALISTORE–European Research Institute, FR CNRS 3104, 80039 Amiens, France. <sup>3</sup>Réseau sur le Stockage Electrochimique de l'Énergie (RS2E), FR CNRS 3459, France. <sup>4</sup>National Institute of Chemistry, Hajdrihova 19, SI-1000 Ljubljana, Slovenia. <sup>5</sup>Electron Microscopy for Materials Science (EMAT), University of Antwerp, Groenenborgerlaan 171, B-2020, Antwerp, Belgium. <sup>6</sup>Center for Electrochemical Energy Storage, Skolkovo Institute of Science and Technology, 3 Nobel Street, 143026 Moscow, Russia. <sup>7</sup>Institut Charles Gerhardt, CNRS UMR 5253, Université Montpellier, Place Eugène Bataillon, 34 095 Montpellier, France. <sup>8</sup>IPREM/ECP (UMR 5254), University of Pau, 2 Avenue Pierre Angot, 64053 Pau Cedex 9, France. <sup>9</sup>Electrochemistry Laboratory, Paul Scherrer Institut, CH-5232 Villigen PSI, Switzerland. <sup>10</sup>Sorbonne Universités–UPMC Univ Paris 06, 4 Place Jussieu, F-75005 Paris, France. \*Corresponding author. E-mail: jean-marie.tarascon@college-de-france.fr



This transformation indicates the presence of either a solid solution during the removal of lithium or a broad energy distribution of the lithium sites. By contrast, the  $\text{Li}_2\text{IrO}_3$  sample shows that the plateaus seen on first charge are far more robust, as reported by Kobayashi *et al.* (23). However, the  $dy/dV$  curves show a steady decrease in the size of the redox peaks with extended cycling, yielding a substantial capacity fade for both samples; the  $x = 0$  composition in particular shows none of the voltage fade seen in many Li-rich oxides (3, 14).

Because the  $x = 0$  and 0.25 samples behave differently, the structural evolution was studied in detail for both systems. Figure 1E shows the associated changes in the XRD patterns for the  $x = 0.25$  sample during extended cycling. At the end of charge, the XRD pattern indexes to that of an O1-type structure with a hexagonal close-packed stacking (right image in Fig. 1A). After the first cycle, the XRD pattern returns primarily to that of the pristine O3 structure, though with the appearance of a few small new peaks. These peaks grow with extended cycling until only they remain after 50 cycles, and the peaks attributed to the O3 structure are no longer present. This same process occurs in  $\text{Li}_2\text{IrO}_3$  samples (fig. S3).

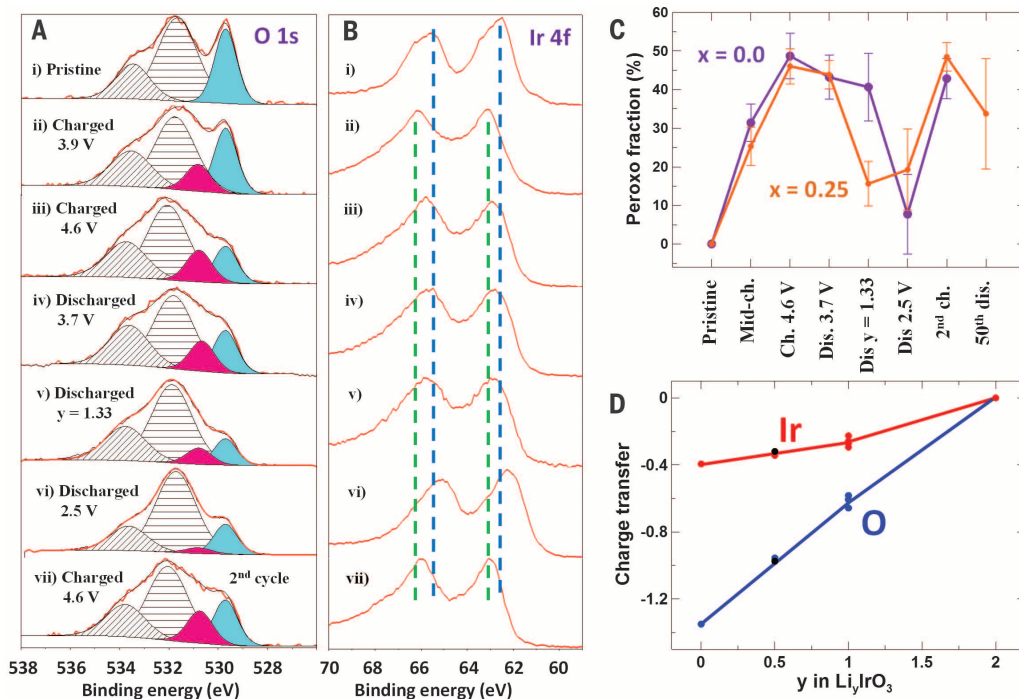
Figure 2 covers the redox processes that occur during electrochemical cycling. The x-ray photoelectron spectroscopy (XPS) results shown in Fig. 2, A and B, and fig. S4 are consistent with previous results for Ru-based systems (13–15) wherein both metal and oxygen oxidations take place during charge. Here, Ir begins in the 4+ state and is oxidized during the first plateau, which ends at 3.9 V. This represents the greatest positive shift in the Ir 4f peak, and it is tempting to attribute

this shift to  $\text{Ir}^{5+}$ , based on the fact that nearly 1 Li atom is removed from  $\text{Li}_2\text{IrO}_3$  ( $x = 0$ ) and 0.75 is removed from  $\text{Li}_2\text{Ir}_{0.75}\text{Sn}_{0.25}\text{O}_3$  ( $x = 0.25$ ), as shown in Fig. 1C. However, unlike in Ru-based systems, we can already detect the presence of peroxo-like species in the O 1s peaks in the XPS spectra at mid-charge, as shown in Fig. 2A ( $x = 0$ ) and fig. S4 ( $x = 0.25$ ). **This suggests a mixed redox process, such that Ir is not strictly in the 5+ state but instead the electron being removed during charge is taken from both Ir and O, which is expected given the highly covalent Ir-O bond.** Figure 2C shows the progression of the fraction of oxygen in the peroxo-like species during cycling for both samples. In each case, the fully charged state contains nearly half of the sample's oxygen in the peroxo-like species  $\text{O}_2^{n-}$ . Upon discharge, the peroxo-like species is reduced back to  $\text{O}^{2-}$  between 3.7 and 2.5 V for both samples, though it occurs slightly earlier in discharge for the Sn-containing material where the peroxo-like species is reduced by the time a lithium content of 1.33 atoms is reached. This difference suggests that Sn promotes the reversibility of the anionic redox process over a wider potential window (3.7 to 3.25 V) with less hysteresis. This change may be attributed to added flexibility in the oxygen network due to the presence of Sn, as previously proposed (13). The  $\text{Li}_2\text{IrO}_3$  sample is therefore a Li-rich oxide, where the peroxo-like species are seen by XPS without immediate conversion to an S curve in the cycling data. We therefore have the opportunity to study anionic redox and the conversion to S curve independently and to establish the true cause of the transformations seen in other Li-rich oxides. Figure 2D shows the change in Bader

charge calculated with density functional theory (DFT) as Li is removed from  $\text{Li}_2\text{IrO}_3$ . This also shows mixed redox throughout the Li extraction, in agreement with the XPS results.

These results imply that the local distortions in the oxygen lattice associated with the formation of peroxo-like species can be observed directly by transmission electron microscopy (TEM). The reason such information is available for the  $\text{Li}_2\text{IrO}_3$  system is that the charged sample takes an O1 structure (Fig. 1A, refinements shown in fig. S5, and structure given in table S2) such that the projection of the oxygen columns becomes available along the  $c$  axis without overlapping with the columns of Ir or Li. The [010], [100], and [001] high-angle annular dark-field scanning transmission electron microscopy (HAADF-STEM) images of the charged  $\text{Li}_{0.5}\text{IrO}_3$  sample show the highly ordered O1 structure viewed across (Fig. 3A and fig. S6, left) and along (Fig. 3B and fig. S6, right) the  $c$  axis. These images demonstrate perfect honeycomb ordering of the Ir cations on the transition metal layer and very little migration of Ir to the now nearly empty Li layer. This highly ordered structure is very unusual for this class of Li-rich layered oxides and allows for visualization of the oxygen columns using annular bright field STEM (ABF-STEM) imaging (Fig. 3, B and C, and fig. S7). The ABF-STEM technique has been proven to accurately reveal the positions of “light” elements (such as Li, O, and even H) in the presence of atomic entities with much higher scattering power (24–27). The correspondence between the experimental [001] HAADF- and ABF-STEM images and the crystal structure projection was established with the help of the simulated

**Fig. 2. Changes in cationic and anionic oxidation states during  $\text{Li}_2\text{IrO}_3$  cycling.** (A) Oxygen 1s core XPS peaks at various points after electrochemical cycling. The  $\text{O}^{2-}$  (blue) and  $\text{O}_2^{n-}$  (red) peaks are attributed to the sample, whereas the two gray striped peaks represent the surface species and electrolyte decomposition products, as described in (13). (B) Iridium 4f core XPS peaks. The dashed lines are guides for the eye indicating the position of the pristine (4+) peaks (blue) and the highest oxidation state (5+) (green). (C) Fraction of lattice oxygen attributed to peroxo for  $\text{Li}_{1-x}\text{Ir}_x\text{O}_3$  samples. The samples discharged to  $y = 1.33$  were stopped at 3.4 V for  $\text{Li}_2\text{IrO}_3$  and 3.25 V for  $\text{Li}_2\text{Ir}_{0.75}\text{Sn}_{0.25}\text{O}_3$ , as shown in Fig. 1C. (D) Results for change in Bader charge with respect to the pristine sample obtained from DFT calculations. These are consistent with the XPS results showing mixed redox throughout the charge process. All calculations were performed on the O3 structure, except for the black points at  $y = 0.5$ , which were obtained for the O1 structure. The red and blue lines are guides for the eye and illustrate continuous mixed redox during charge.



images, using the crystallographic data in table S2 (fig. S8). The projected symmetry of the  $\text{IrO}_6$  octahedra is expected to be close to sixfold symmetry, corresponding to all nearly equal O-O separations. However, the shape of these octahedra in the experimental [001] ABF-STEM image is clearly driven toward threefold symmetry due to the formation of shortened (black dumbbells) and lengthened (left blank) projected O-O separations (Fig. 3C). The distinct difference in the short and long O-O projected separations is evident from a comparison of the corresponding ABF intensity profiles (Fig. 3D). The values of the projected O-O separations were estimated from the analysis of a histogram of their distribution (fig. S11), which demonstrates peaks centered at 1.56 and 1.83 Å, reflecting the average values of the shortened and lengthened projected O-O distances (Table 1).

The observed distortion of the oxygen sublattice is in line with the atomic arrangement obtained from ab initio calculations. Figure 3E shows the [001] projection, as obtained on the basis of DFT calculations for the charged  $\text{Li}_{0.5}\text{IrO}_3$  sample. This calculation shows shortened pro-

jected O-O distances for pairs of oxygen atoms (joined by red lines) lying between two Ir atoms. Figure 3E also shows the Fukui function, which probes the change in the electron density as a result of an infinitesimal change in the total number of electrons. The Fukui function can be used to probe the redox-active center (atomic and/or molecular entities affected by the charge variation; i.e., where the electronic charge is varying) in an electrochemical reaction. Here, the Fukui function shows changes in electron density around both Ir and O. The shape of the Fukui function around the oxygen atom shows overlapping lobes along the axis joining the O-O pairs with short separations, consistent with the expectation of partially empty antibonding  $\sigma^*$  orbitals if peroxo-like species are formed. By contrast, fig. S9 shows no such orbital overlap in the pristine material.

The distortion pattern observed on a local scale was confirmed using the structural refinements of the bulk structure from neutron powder diffraction (NPD) data for the pristine and fully charged Li-Ir-O samples (included in figs. S5 and S10). The [001] projections of the refined structures are shown overlaid in Fig. 3F (for this

image, the unit cell of the pristine structure was shrunk slightly to overlap but the aspect ratio was not changed). This shows the displacement in the oxygen lattice taking place during the formation of the peroxo-like species and is consistent with the ABF-STEM image. This also serves to show that changes seen in projected distance with ABF-STEM do in fact correspond to actual atomic displacements.

Table 1 presents a summary of the O-O distances determined with different methods, all confirming a distortion in the lattice such that oxygen atoms approach each other to form O-O pairs lying between two adjacent Ir atoms. By contrast, no such distortions have been seen for materials that do not involve anionic redox [e.g., the stoichiometric NMC compounds given in Table 1 with values based on neutron diffraction (28)]. However, the O-O distances measured here do not approach the  $\sim 1.5$  Å O-O distances seen for peroxide species in highly ionic compounds, such as  $\text{Li}_2\text{O}_2$ , or in systems where oxygen pairs lie in cavities within the cationic network, as seen in a few perovskite materials (29). In more covalent systems, such as those discussed here, the formation

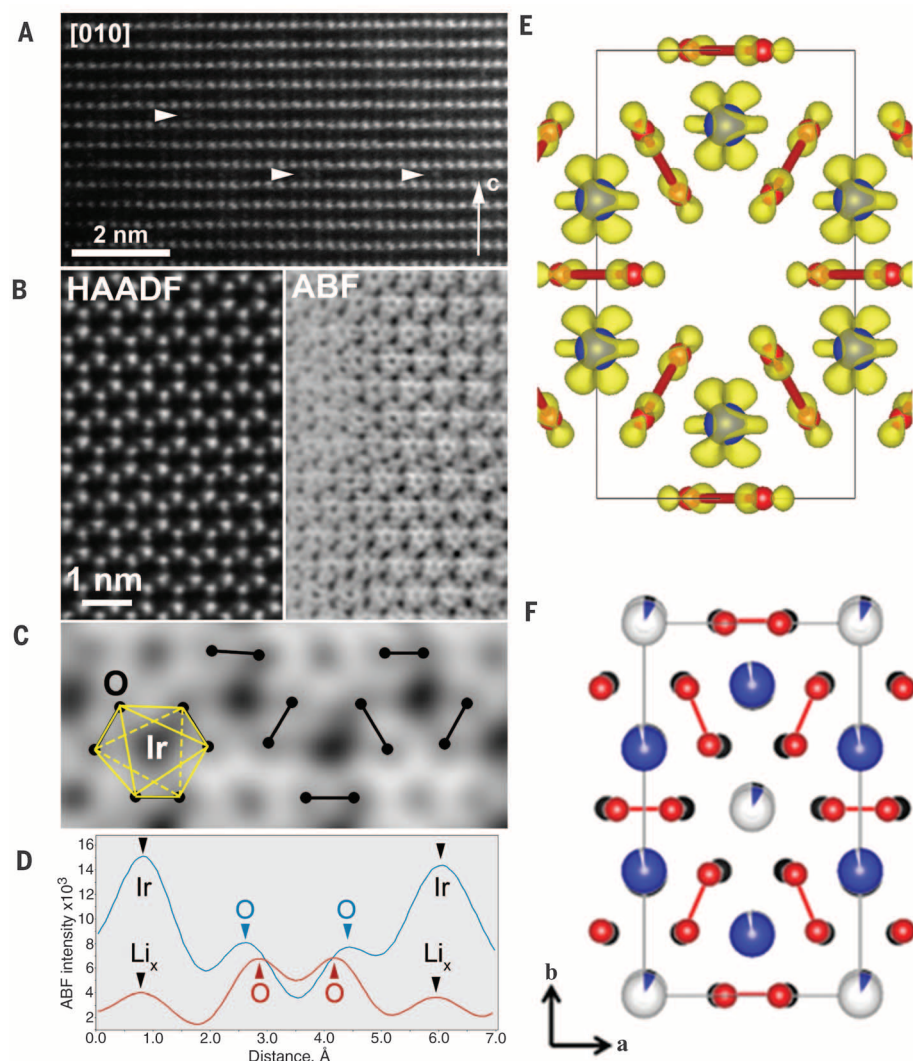


**Fig. 3. Structural changes in the oxygen sublattice.** (A) [010] HAADF-STEM image of the charged  $\text{Li}_{0.5}\text{IrO}_3$  sample, demonstrating the ordered sequence of the Ir layers corresponding to the O1-type structure. The hexagonal close-packing is evident from the absence of the lateral displacement of layers. Virtually no migration of the Ir cation to the Li layers is observed; a few antisite point defects are marked with arrowheads. (B) [001] HAADF-STEM and ABF-STEM images of the same sample (taken from different areas; the noise in the ABF-STEM image is suppressed by applying a low-pass Fourier filter). (C) Enlarged ABF-STEM image. O-O pairs with short projected distances are marked with dumbbells. The O-O pairs arise from twisting the opposite triangular faces of the  $\text{IrO}_6$  octahedra (shown in yellow). (D) ABF intensity profiles along the O-O pairs with long (blue) and short (red) projected distances. (E) [001] projection of the  $\text{Li}_{0.5}\text{IrO}_3$  in the O1 stacking configuration, obtained with DFT calculations. Li atoms are omitted for clarity, oxygen atoms are shown in red, and Ir atoms are in blue. The yellow surfaces are the Fukui orbitals. (F) Structure of the charged Li-Ir-O material, as obtained from neutron powder diffraction (fit shown in fig. S5), overlaid on the pristine structure (fit in fig. S10) shown in black, clearly illustrating the formation of O-O dimers. The overlay required shrinking the pristine structure slightly, but the aspect ratio was unaltered.



of peroxy species therefore manifests itself as a distortion of the oxygen framework with the formation of shorter and longer O-O distances. An important aspect of these materials is the extent to which they allow O<sub>2</sub> recombination and subsequent oxygen gas release during oxidation, which must be minimized to reduce the irreversible capacity loss. Figure S12 shows that the oxygen release here is relatively small, especially for Li<sub>2</sub>IrO<sub>3</sub>, and only occurs at voltages above 4.3 V versus Li/Li<sup>+</sup>, consistent with our previous studies (13, 16, 19). This voltage corresponds to ~1.3 V versus standard hydrogen electrode, very close to the potential at which water is split (1.23 V). Our value is a rough estimate, but it does suggest that peroxy-species will be stable against forma-

tion of oxygen gas if they form below 4.3 V. This explains why irreversible capacities have plagued the Li-rich NMC materials, which must be oxidized up to 4.5 V to convert to an S curve. Figure 4 shows a steady decrease in capacity (with no associated voltage fade) during extended cycling, with ~50% retention after only 50 cycles. This fade coincides with the structural variations resulting in the changes to the XRD patterns in Fig. 1. Figure 4 shows the structural changes that occur during extended cycling, as visualized with HAADF-STEM imaging. The image collected after 50 cycles is very unusual, with an apparent nanoscale intergrowth of two distinct structures. The structural changes during electrochemical cycling

that involve the gliding of (Ir<sub>1-x</sub>Sn<sub>x</sub>)<sub>2/3</sub>O<sub>2</sub> slabs against each other are ultimately detrimental to the long-term cycling of this material, thus giving rise to capacity fade without any of the voltage fade seen in other Li-rich materials. This demonstrates that these two parameters for evaluating battery performance are not directly related here and that although the transformation from O3 to O1 structures prevents voltage fade, it still results in detrimental capacity fade.

Our NPD and DFT results suggest that peroxy-like dimers form uniformly throughout the bulk in the fully charged Li<sub>0.5</sub>IrO<sub>3</sub> material, allowing us to determine the possible limits on the value of the formal charge *n* for peroxy-like O<sub>2</sub><sup>*n*-</sup> dimers. The lower bound can be set by assuming that all of the 1.5 Li atoms transferred per O<sub>3</sub> unit are attributed to oxygen redox only; this yields *n* = 3.0. The upper bound is set by assuming the mixed redox obtained by DFT calculations (and confirmed qualitatively with XPS), in which case the oxygen lattice accounts for ~1.0 Li atom removed per O<sub>3</sub> unit, resulting in *n* = 3.3. This study therefore suggests the formation of predominantly O<sub>2</sub><sup>3-</sup> species in Li-rich layered oxides, which explains why all of the lithium cannot be systematically removed from these materials simply by fully oxidizing the oxygen, as would be the case if *n* = 2 was accessible. This also explains why the peroxy-like species were detected by electron paramagnetic resonance (EPR) (13, 30), given that O<sub>2</sub><sup>2-</sup> is EPR silent whereas O<sub>2</sub><sup>3-</sup> is active.

The fact that the formation of peroxy-like dimers does not necessarily imply antisite cation disordering has a few consequences. In Li<sub>2</sub>IrO<sub>3</sub>, the displacement of oxygen atoms during first charge results in confining the space around the iridium atom (Fig. 3F). This results in less free volume around each iridium atom and more tight binding to the surrounding oxygen atoms, therefore lending support to the fact that little migration of iridium takes place and no conversion to the S curve is seen. By contrast, the disorder caused by the addition of tin locally disrupts the pattern of the O<sub>2</sub><sup>*n*-</sup> species promoting such migration, which results in a far greater abundance of the antisite defects in the [010] HAADF-STEM images of the charged *x* = 0.25 sample (fig. S13). Thus, conversion to an S curve is seen. More generally, once the Li is removed from the transition metal layers in all Li-rich oxides, the created free volume promotes migration to the Li layer. The microscopy images for this model system also show that these high capacities can be achieved for single-phase layered materials and do not necessarily require structural intergrowth of two layered phases, as proposed in the past (3). Lee *et al.* (31) showed Li-rich Li-Cr-Mo-O materials that convert toward a disordered rock salt structure during charge (corresponding to massive cation migration such that the transition metal and lithium layers are indistinguishable). Unfortunately, this study did not examine the redox processes involved, and we propose that this material is simply another example of the Li-rich oxides where oxygen participation in the redox process leads to high capacities.

**Table 1. Average O-O distances obtained by DFT, NPD, and TEM.** “Short” refers to two oxygen atoms between two nearest-neighbor Ir atoms, as viewed in the [001] projection in Fig. 3, E and F. “Long” refers to distances at which the oxygen atoms lie between an Ir atom and a vacancy. In all cases, the distances are averages for the structure. Projected distances are shown for the O1 structure only. N/A, not applicable; ND, not determined.

Sample	O-O distance (Å)		O-O distance in [001] projection (Å)	
	Short	Long	Short	Long
<hr/>				
Li <sub>2</sub> IrO <sub>3</sub>				
Neutron	2.77(2)	2.84(2)	N/A	N/A
DFT	2.74	2.89	N/A	N/A
<hr/>				
Li <sub>0.5</sub> IrO <sub>3</sub>				
Neutron	2.45(2)	2.73(4)	1.42(1)	1.86(3)
DFT	2.54	2.77	1.51	1.88
TEM	ND	ND	1.56	1.83
<hr/>				
LiNi <sub>1/3</sub> Mn <sub>1/3</sub> Co <sub>1/3</sub> O <sub>2</sub> *	2.686	2.686	N/A	N/A
Li <sub>0.04</sub> Ni <sub>1/3</sub> Mn <sub>1/3</sub> Co <sub>1/3</sub> O <sub>2</sub> *	2.553	2.553	N/A	N/A

\*From (28), as an indication of behavior in systems where redox involves the cationic species only.

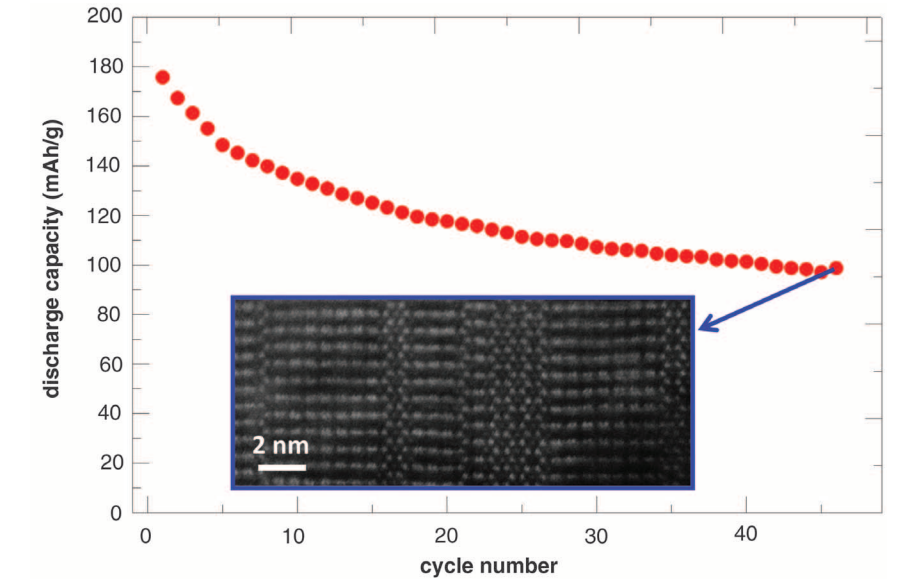


**Fig. 4. Long-term cycling performance.** Discharge capacity during extended cycling for Li<sub>2</sub>Ir<sub>0.75</sub>Sn<sub>0.25</sub>O<sub>3</sub>. (Inset) [100] HAADF-STEM image of a particle obtained after 50 cycles, showing complex nanoscale structuring.

Metal substituents can be used to tune the physical properties of these Li-rich phases because they affect the  $(\text{O}_2)^{n-}$  stability against oxygen recombination or voltage fade, as previously demonstrated for  $\text{Li}_2\text{Ru}_{1-x}\text{M}_x\text{O}_3$  ( $\text{M} = \text{Sn}, \text{Ti}, \text{Mn}$ ). The benefits of Sn, in that it limits both  $\text{O}_{2(g)}$  release and voltage fade, are preserved in the  $\text{Li}_2\text{Ir}_{1-y}\text{Sn}_y\text{O}_3$  system but are mitigated by the emergence of a capacity fade mechanism that is linked to the emergence and accumulation of stacking faults. This finding emphasizes that the origins of voltage and capacity fading in these Li-rich layered phases are different, a point that has previously been a source of confusion.

In summary, combined TEM, neutron diffraction, and ab initio studies on high-capacity Li-rich  $\text{Li}_2\text{Ir}_{1-x}\text{Sn}_x\text{O}_3$  layered phases permitted the atomic-scale visualization of the  $(\text{O}-\text{O})^{n-}$  peroxo-like dimers responsible for the capacity gain in Li-rich layered electrode materials. These observations lead to a better understanding of peroxo formation and localization,  $\text{O}_2$  recombination, and the effect of the transition metal substituents. Additionally, these findings provide a chemical handle for tuning the performances of Li-rich layered materials.

## REFERENCES AND NOTES

- B. L. Ellis, K. T. Lee, L. F. Nazar, *Chem. Mater.* **22**, 691–714 (2010).
- Z. Lu, L. Y. Beaulieu, R. A. Donaberg, C. L. Thomas, J. R. Dahn, *J. Electrochem. Soc.* **149**, A778 (2002).
- M. M. Thackeray, C. S. Johnson, J. T. Vaughey, N. Li, S. A. Hackney, *J. Mater. Chem.* **15**, 2257–2267 (2005).
- J. M. Tarascon et al., *J. Solid State Chem.* **147**, 410–420 (1999).
- G. Ceder et al., *Nature* **392**, 694–696 (1998).
- M. K. Aydinol, A. F. Kohan, G. Ceder, K. Cho, J. Joannopoulos, *Phys. Rev. B* **56**, 1354–1365 (1997).
- C.-C. Chang, O. I. Veilikhatnyi, P. N. Kumta, *J. Electrochem. Soc.* **151**, J91–J94 (2004).
- J. Graetz, C. C. Ahn, R. Yazami, B. Fultz, *J. Phys. Chem. B* **107**, 2887–2891 (2003).
- S. Laha et al., *Phys. Chem. Chem. Phys.* **17**, 3749–3760 (2015).
- H. Koga et al., *J. Phys. Chem. C* **118**, 5700–5709 (2014).
- M. Oishi et al., *J. Power Sources* **276**, 89–94 (2015).
- W.-S. Yoon et al., *J. Phys. Chem. B* **106**, 2526–2532 (2002).
- M. Sathiyar et al., *Nat. Mater.* **12**, 827–835 (2013).
- M. Sathiyar et al., *Nat. Mater.* **14**, 230–238 (2015).
- M. Sathiyar et al., *Chem. Mater.* **25**, 1121–1131 (2013).
- E. McCalla et al., *J. Electrochem. Soc.* **162**, A1341–A1351 (2015).
- J. Rouxel, *Chem. Eur. J.* **2**, 1053–1059 (1996).
- M. Sathiyar et al., *Chem. Commun.* **49**, 11376–11378 (2013).
- E. McCalla et al., *J. Am. Chem. Soc.* **137**, 4804–4814 (2015).
- A. R. Armstrong et al., *J. Am. Chem. Soc.* **128**, 8694–8698 (2006).
- N. Yabuuchi et al., *Proc. Natl. Acad. Sci. U.S.A.* **112**, 7650–7655 (2015).
- Materials and methods are available as supplementary materials on Science Online.
- H. Kobayashi, M. Tabuchi, M. Shikano, H. Kageyama, R. Kanno, *J. Mater. Chem.* **13**, 957–962 (2003).
- S. D. Findlay et al., *Ultramicroscopy* **110**, 903–923 (2010).
- R. Ishikawa et al., *Nat. Mater.* **10**, 278–281 (2011).
- L. Gu, D. Xiao, Y.-S. Hu, H. Li, Y. Ikuhara, *Adv. Mater.* **27**, 2134–2149 (2015).
- D. Batuk, M. Batuk, A. M. Abakumov, J. Hadermann, *Acta Crystallogr. B* **71**, 127–143 (2015).
- S. C. Yin, Y. H. Rho, I. Swainson, L. F. Nazar, *Chem. Mater.* **18**, 1901–1910 (2006).
- F. Grasset, C. Dussarrat, J. Darriet, *J. Mater. Chem.* **7**, 1911–1915 (1997).
- M. Sathiyar et al., *Nat. Commun.* **6**, 6276 (2015).
- J. Lee et al., *Science* **343**, 519–522 (2014).

## ACKNOWLEDGMENTS

E.M. thanks the Fonds de Recherche du Québec-Nature et Technologies and ALISTORE-European Research Institute for funding this work, as well as the European community I3 networks for funding the neutron scattering research trip. This work was also funded by the Slovenian Research Agency research program P2-0148. This work is partially based on experiments performed at the Institut Laue Langevin. We thank J. Rodriguez-Carvajal for help with neutron scattering experiments and for fruitful discussions. We also thank M. T. Sougrati for performing the Sn-Mössbauer measurements. Use of the Advanced Photon Source at Argonne National Laboratory was supported

by the U.S. Department of Energy, Office of Science, Office of Basic Energy Sciences, under contract no. DE-AC02-06CH11357. M.S. and M.-L.D. acknowledge high-performance computational resources from GENCI-CCRT/CINES (grant cmm6691). J.-M.T. acknowledges funding from the European Research Council (ERC) (FP/2014-2020)/ERC Grant-Project670116-ARPEMA.

## SUPPLEMENTARY MATERIALS

www.sciencemag.org/content/350/6267/1516/suppl/DC1  
Materials and Methods  
Figs. S1 to S13  
Tables S1 and S2  
References (32–43)

19 June 2015; accepted 6 November 2015  
10.1126/science.aac8260

## PLANT SYMBIOSES

# Rice perception of symbiotic arbuscular mycorrhizal fungi requires the karrikin receptor complex

Caroline Gutsch, <sup>1,2\*</sup> Enrico Gobbato, <sup>3\*</sup> Jeongmin Choi, <sup>3</sup> Michael Riemann, <sup>4,5</sup> Matthew G. Johnston, <sup>3</sup> William Summers, <sup>3</sup> Samy Carbonnel, <sup>2</sup> Catherine Mansfield, <sup>3</sup> Shu-Yi Yang, <sup>1</sup> Marina Nadal, <sup>1</sup> Ivan Acosta, <sup>6</sup> Makoto Takano, <sup>4</sup> Wen-Biao Jiao, <sup>6</sup> Korbinian Schneeberger, <sup>6</sup> Krystyna A. Kelly, <sup>3</sup> Uta Paszkowski <sup>1,3†</sup>

In terrestrial ecosystems, plants take up phosphate predominantly via association with arbuscular mycorrhizal fungi (AMF). We identified loss of responsiveness to AMF in the rice (*Oryza sativa*) mutant *hebiba*, reflected by the absence of physical contact and of characteristic transcriptional responses to fungal signals. Among the 26 genes deleted in *hebiba*, *DWARF 14 LIKE* is, the one responsible for loss of symbiosis. It encodes an alpha/beta-fold hydrolase, that is a component of an intracellular receptor complex involved in the detection of the smoke compound karrikin. Our finding reveals an unexpected plant recognition strategy for AMF and a previously unknown signaling link between symbiosis and plant development.

Most land plants establish symbioses with arbuscular mycorrhizal fungi (AMF) of the phylum *Glomeromycota* (1). These symbioses contribute to global carbon and mineral nutrient cycles, because AMF provide mineral nutrients to the plant and receive carbohydrates in return. Colonization of plant roots by AMF requires reciprocal recognition initiated by diffusible molecules before fungal

attachment to the root surface and root penetration via hyphopodia (2). Diffusible precolonization signals include strigolactones, released from plant roots that activate the fungus before physical interaction (3), and fungal (lipo)chitooligosaccharides and chitotetraose, secreted by AMF that trigger plant calcium signaling, gene expression, and lateral root formation (4, 5). Plant LysM receptor-like kinases (6) are required for perception of chitinaceous microbial molecules that trigger either symbiosis or defense signaling (7–9). Plant signaling mutants impaired in root colonization by both AMF and nitrogen-fixing bacteria still exhibit transcriptional responses to fungal signaling molecules (10–12). Therefore, additional signaling modules have been postulated (12). We identified the rice receptor for karrikin, a plant growth regulator first identified in smoke (13–16), as a necessary signaling component for establishment of arbuscular mycorrhizal (AM) symbiosis.

We found that the jasmonate-deficient rice (*Oryza sativa*) mutant *hebiba* (17) was unable to

<sup>1</sup>Department of Plant Molecular Biology, University of Lausanne, Biophore Building, 1015 Lausanne, Switzerland.  
<sup>2</sup>Faculty of Biology, Genetics, University of Munich, Biocenter Martinsried, Grosshaderner Straße 2-4, 82152 Martinsried, Germany.  
<sup>3</sup>Department of Plant Sciences, University of Cambridge, Downing Street, Cambridge CB2 3EA, UK.  
<sup>4</sup>Division of Plant Sciences, National Institute of Agrobiological Sciences, 2-1-2 Kannondai, Tsukuba, Ibaraki 305-8602, Japan.  
<sup>5</sup>Botanical Institute, Molecular Cell Biology, Karlsruhe Institute of Technology, Kaiserstraße 2, 76131 Karlsruhe, Germany.  
<sup>6</sup>Max Planck Institute for Plant Breeding Research, Carl-von-Linné-Weg 10, D-50829 Cologne, Germany.

\*These authors contributed equally to this work.

†Corresponding author. E-mail: up220@cam.ac.uk



# Visualization of O-O peroxo-like dimers in high-capacity layered oxides for Li-ion batteries

Eric McCalla, Artem M. Abakumov, Matthieu Saubanère, Dominique Foix, Erik J. Berg, Gwenaëlle Rousse, Marie-Liesse Doublet, Danielle Gonbeau, Petr Novák, Gustaaf Van Tendeloo, Robert Dominko and Jean-Marie Tarascon (December 17, 2015) *Science* **350** (6267), 1516-1521. [doi: 10.1126/science.aac8260]

Editor's Summary

## Peering into cathode layered oxides

The quest for better rechargeable batteries means finding ways to pack more energy into a smaller mass or volume. Lithium layered oxides are a promising class of materials that could double storage capacities. However, the design of safe and long-lasting batteries requires an understanding of the physical and chemical changes that occur during redox processes. McCalla *et al.* used a combination of experiments and calculations to understand the formation of O-O dimers, which are key to improving the properties of these cathode materials.

*Science*, this issue p. 1516

---

This copy is for your personal, non-commercial use only.

---

### Article Tools

Visit the online version of this article to access the personalization and article tools:  
<http://science.sciencemag.org/content/350/6267/1516>

### Permissions

Obtain information about reproducing this article:  
<http://www.sciencemag.org/about/permissions.dtl>

*Science* (print ISSN 0036-8075; online ISSN 1095-9203) is published weekly, except the last week in December, by the American Association for the Advancement of Science, 1200 New York Avenue NW, Washington, DC 20005. Copyright 2016 by the American Association for the Advancement of Science; all rights reserved. The title *Science* is a registered trademark of AAAS.